Lithium Niobate Nanocubes as Linear and Nonlinear Ultraviolet Mie Resonators

Flavia Timpu,[1] Joan Sendra,[1⊥] Claude Renaut,[1] Lukas Lang,[1] Maria Timofeeva,[1] Maria Teresa Buscaglia,[2] Vincenzo Buscaglia,[2] and Rachel Grange[1]*

[1]Optical Nanomaterial Group, Institute for Quantum Electronics, Department of Physics, ETH Zürich, Auguste-Piccard- Hof 1, 8093 Zürich, Switzerland

[2]Institute of Condensed Matter Chemistry and Technologies for Energy, National Research Council, Via De Marini 6, I-16149 Genoa, Italy

[⊥]Current address: ETH Zurich, Laboratory for Nanometallurgy, Vladimir Prelog Weg 1-5/10, 8093 Zürich, Switzerland

*Corresponding author: ftimpu@phys.ethz.ch

Abstract

Many dielectrics and semiconductors used for all-dielectric resonators or metasurfaces have low absorption in the visible range down to 500 nm, but are lossy in the near ultraviolet (NUV) range due to their low energy band gap. On the contrary, the dielectric ferroelectric lithium niobate ($LiNbO_3$, LNO) has an energy band gap larger than 4 eV, and consequently, very low losses in the NUV range down to 310 nm. We propose LNO nanocubes as a new alternative material for nonlinear photonics in the NUV range. We report that LNO nanocubes fabricated by solvothermal synthesis with sizes from 200 to 300 nm ~~offer different optical features compared to typical all-dielectric resonators. The LNO nanocubes are efficient nanostructures for light manipulation in the NUV range. They~~ demonstrate strong second harmonic generation (SHG) emission below 400 nm due to Mie resonances, with an SHG enhancement of 10^7 compared to bulk LNO at 360 nm. The LNO nanocubes presented in this work are novel efficient all-dielectric Mie resonant nanostructures for the NUV with a wide range of possible photonics applications in the NUV range, from nanophotolithography to metasurfaces and complex assemblies of nanostructures.

TOC (Table of contents) Graphic:

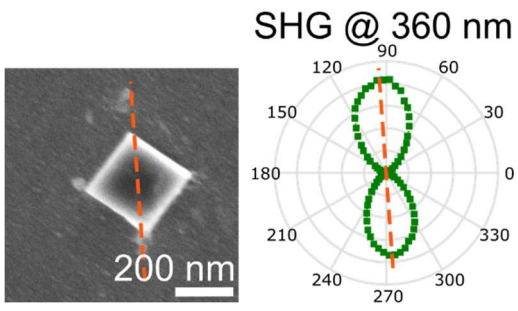

Keywords: near ultraviolet; nanophotonics; second-harmonic generation; Mie scattering; lithium niobate;

Introduction

~~The development of photonics was marked by the invention of the laser and the subsequent demonstration of nonlinear optical phenomena. Sum frequency generation signals, in particular second harmonic generation (SHG), are utilized in many applications such as optical communication, optical parametric generation and amplification, and the development of multiphoton microscopy.~~

The development of photonics was marked by the invention of the laser and the subsequent demonstration of nonlinear optical phenomena, such as sum- and difference-frequency generation, third harmonic generation or optical parametric generation. These nonlinear phenomena are utilized in many applications from optical communication and optical parametric amplification to the development of multiphoton microscopy.[1]

~~In bulk materials the nonlinear conversion efficiency is affected by phase matching due to the dispersion of light. Periodic poling, quasi-phase matching and random phase matching are proposed solutions which lead to higher conversion efficiencies independent of the length of the nonlinear material. Another way to overcome the limitation of phase matching is to use structures with sizes smaller than the coherence length. Nanometer sized optical materials also have an additional advantage: due to their limited size, they locally confine the electromagnetic field at specific wavelengths that can be tuned by changing the size, shape and material. Moreover, these nanostructures have complex linear extinction spectra containing several electric and magnetic multipole resonances that lead to the enhancement of light-matter interaction and nonlinear signal emission efficiency, as well as the suppression of the linear scattering cross-section in anapole-like modes.~~ In bulk materials, the wave propagation is linked to the wavelength dependent refractive index. Hence, the nonlinear emission efficiency is high when phase matching conditions

are fullfiled.[2] Several solutions are proposed to achieve phase matching in a material, such as periodic poling,[3] quasi-phase matching[2] or random phase matching.[4] Conversely, the phase mismatch can also be reduced if the refractive index of the material is close to zero. This exotic behavior is obtained in zero-index metamaterials, which are fabricated by structuring metal-dielectric composites at the subwavelength level.[5] Nanostructuring of bulk materials opened the way to photonic devices with new properties. In addition to metamaterials with exotic dielectric functions, nanostructuring is used to miniaturize optical components such as lenses, filters, polarizers with tunable, switchable or sensing functionalities.[6–8] The nanostructures forming these metamaterials have sizes smaller than the coherence length. Consequently, phase matching techniques are not necessary and have no effect on their nonlinear emission efficiency. On the other hand, nanostructures locally confine electromagnetic fields due to their limited size. This confinement occurs at specific wavelengths that can be tuned by changing the size, shape and material. Therefore, nanostructures have complex linear extinction spectra containing several electric and magnetic multipole resonances[9] that are used to enhance light-matter interaction and nonlinear signal emission efficiency,[10–16] as well as the suppression of the linear scattering cross-section in anapole-like modes.[17–19]

Metallic nanostructures with asymmetrical geometrical shapes have been successfully used as nonlinear emitters.[20–23] While such plasmonic nanostructures are rather easy to fabricate, their use is limited in the visible (VIS) range due to high ohmic losses. [24] ~~their main disadvantage are their high ohmic losses in the visible range.~~[24] Furthermore, noble metals have a centrosymmetric crystal structure and their second order nonlinear optical properties originate only from the broken symmetry at the surface[20,21] or from higher-order multipole resonance effects.[23] Nanostructures fabricated from high refractive index dielectric materials such as silicon (Si), gallium arsenide

(GaAs) or germanium (Ge) have been proposed as an alternative without the ohmic losses of metals.[25–29]. ~~Even if these materials possess much lower losses in the visible and near infrared range,~~ However, none of these materials possess bulk second order nonlinearities and low losses in the VIS range at the same time. Furthermore, their performance reduces even more in the near ultraviolent (NUV) range due to absorption coefficients higher than 1 at 350 nm.[30,31] In conclusion, new second order nonlinear materials for applications in the NUV-VIS range are required.

In this work, we propose to use ferroelectric dielectric metal oxide lithium niobate ($LiNbO_3$, LNO) nanostructures as an ~~alternative~~ new material for nonlinear photonic application in the NUV-VIS range. In its bulk form, LNO is a transparent insulating material with a high energy bandgap of 4 eV[32] and an absorption coefficient smaller than 10^{-5} at 350 nm.[33] Additionally, LNO has a hexagonal noncentrosymmetric crystal structure[32,34] with significant nonlinear effects such as piezoelectricity, electro-optical effect and SHG. Due to these nonlinear effects, microstructures and waveguides of LNO are an established material for a number of photonics applications such as SHG, three wave mixing, optical parametric down-conversion or ~~bioimaging and~~ electro-optic effect.[35–39]

On the other hand, few studies were performed on LNO nanostructures. Efforts have been directed towards fabricating nanometer-sized LNO nanostructures, mainly by bottom-up chemical synthesis.[40–48] The crystal structure of these LNO nanostructures is preserved down to diameters as small as 5 nm.[44] Cube-shaped LNO nanoparticles were demonstrated as viable probes for multiphoton imaging of biological samples.[48] Such nanoparticles with nonlinear optical properties, sometimes called harmonic nanoparticles, have been used as coherent subwavelength light emitters or non-resonant microscopy markers.[49–53] Their main advantages compared to fluorescent probes are the lack of bleaching and blinking, the emission of coherent photons, the reduced

nonradiative losses and the natural selectivity. Also, since SHG is strongly linked to the crystal structure of the material, orientation dependent polarization patterns can be measured.[52–56] Additionally, metal oxide nanoparticles are robust and chemically inert in many environments, which makes them biocompatible and non-toxic.[57–60] Harmonic nanoparticles employed in bio-imaging have contributed to overcoming the limitations of various microscopy techniques, leading to improved resolution and detection sensitivity even in deep tissues or turbid media.[49] In the UV range, the biological samples have increased absorption cross-section. This limits the usage of harmonic nanoparticles as markers for bio-imaging, but opens possibilities for applications where high absorptions is desirable, as in the case of teranostics and cancer cell apoptosis.[61] Harmonic nanoparticles are also successfully used to characterize, calibrate and standardize the metrology of multiphoton microscopes with sub-diffraction limit over a broad spectral range.[62]

Given the ~~advantages~~ properties of harmonic nanoparticles listed above, ~~efforts have been directed towards fabricating nanometer-sized LNO structures, mainly by bottom-up chemical synthesis.[40–48] The crystal structure of these nanoparticles is preserved down to diameters as small as 5 nm.[44] Cube-shaped LNO nanoparticles were demonstrated as viable probes for multiphoton imaging of biological samples.[48] Moreover,~~ the low absorption of LNO in the NUV and the high quality of the crystal structure of LNO nanocubes compared to nanospheres,[47] ~~indicate~~ we investigate their potential for further applications in photonics beyond bioimaging as, for instance, new types of metasurfaces,[28,63–65] complex materials, nonlinear light converters[66] or integrated photonics.[36] ~~Here,~~ We show LNO nanocubes as Mie resonators and as efficient SHG emitters, and demonstrate them as novel all-dielectric building blocks for nonlinear nanophotonics in the NUV range. We exploit the larger energy band gap of LNO that makes it transparent down to 310 nm.[32] Furthermore, LNO has an intrinsically non-centrosymmetric hexagonal crystal structure

with a dominant component in the reduced second order susceptibility tensor d_{33} = -34 pm/V.[32] We perform a full spectral characterization of LNO nanocubes with sizes between 200 and 300 nm fabricated by solvothermal synthesis and demonstrate their high SHG efficiency values between ~~1.5~~ 1.7 · 10^{-7} 1/W and ~~6.3~~ 7.6 · 10^{-7} 1/W in the NUV region at 360 nm. Additionally, we show that the SHG from single LNO nanocubes is enhanced 10^7 times compared to bulk LNO. We further show by SHG polarimetry that, compared to nanospheres, LNO nanocubes have predictable SHG emission patterns and crystal orientations when they are deposited with a face parallel to a flat substrate, which allows a better control of the building blocks for future applications.

Results and Discussion

Fabrication of LNO nanocubes

We fabricate LNO powders by a solvothermal synthesis method (see Methods section). We obtain powders containing LNO rhombohedra with sizes ranging from 100 to 400 nm. Examples of single LNO rhombohedra are shown in the SEM micrographs in Figure 1(a). According to XRD measurements (Figure S1(a)), the crystal structure of the LNO rhombohedra corresponds to the hexagonal R3c symmetry. High-resolution TEM images (Figure S1 (b)) reveal that lattice planes with a separation of about 0.38 nm are parallel to the lateral faces of the rhombohedra. This interplanar distance is in good agreement with the value of 0.375 nm expected for the d-spacing of the (012) lattice planes calculated using the reference lattice parameters of LNO, a = 0.5148 nm and c = 1.3863 nm.[34] Because of the 3-fold symmetry of the hexagonal system, the faces of the rhombohedra correspond to three equivalent families of lattice planes, (012), (-102) and (1-12) having the same d-spacing (Figure S1(c)). These planes form an angle of 32.76° with the c-axis,

i.e. the direction of the spontaneous polarization vector.[34] Therefore, the polarization axis of the LNO crystal is oriented along the diagonal of the rhombohedron in such a way that its projection on the lateral faces lies along their major diagonal. From the SEM micrographs, we determine that the angles between the facets of rhombohedra have values of 93.8° and 86.7°, in good agreement with the angles formed by the planes (012), (1-12) and (-102) (Figure S1(d)). For simplicity, and since their width, length and height are almost equal, the LNO rhombohedra are called LNO nanocubes in this work.

The samples for the optical measurements are prepared as follows. We spin coat a diluted suspension of LNO nanocubes powder in ethanol on an ITO covered fused quartz substrate with patterned coordinates. Using dark field microscopy ~~and SEM~~, we locate well-spaced individual nanostructures and we determine by SEM that they are single LNO nanocubes. For the subsequent measurements, we record the positions of only single LNO nanocubes that are at least 10 µm apart from all other structures on the substrate. ~~and~~ We determine their size with SEM (Figure 1(a)) and AFM measurements.

Linear extinction measurements

We measure the linear scattering cross-section of single LNO nanocubes by using a dark field spectroscopy setup that we adapt for an extended detection range in the NUV. The schematic of the UV-extended setup is shown in Figure S2. We equip the body of an inverted transmission microscope with UV compatible optical components. We employ aluminum coated mirrors and we use fused silica lenses to collimate a xenon arc lamp with high emission efficiency in the UV range. We use a 50x apochromat objective to collect the scattered light in order to reduce losses due to the chromatic aberrations of the standard achromat objectives. We detect the linear scattering spectrum with an imaging spectrometer equipped with a CCD camera containing an

extended UV window. ~~The measurement range of this setup is increased down to 350 nm, which includes a 90 nm extension compared to a standard setup (Figure S3).~~

The measured linear scattering cross-section spectra of the LNO nanocubes from Figure 1(a) are shown in Figure 1(b-e). Remarkably, we detect scattering resonances below 400 nm, in the NUV. To better understand the scattering cross-section of the single LNO nanocubes and the nature of the scattering peaks, we perform finite element method (FEM) simulations. The simulation model considers an LNO nanocube on a fused quartz substrate. The length, width and height of the nanocube are set to the values deduced from SEM and AFM micrographs, respectively. The model calculates the scattered field from the LNO nanocube and integrates the Poynting vector over a solid angle corresponding to the numerical aperture of the collection objective. Furthermore, using a FEM model described elsewhere,[17] the expansion of the scattering cross-section into individual spherical harmonics according to Mie theory[9] allows us to calculate the contributions from individual multipoles. The calculated scattering cross-sections for the LNO nanocubes (Cube 1 – 4) are shown in Figure 1(f-i). The numerical simulations show that a strong scattering efficiency is expected below 400 nm for every LNO nanocube, which is confirmed by the linear measurements. Furthermore, an additional peak above 400 nm followed by a shoulder is observed both in the measurements and the simulations for the LNO nanocubes with sizes below 300 nm. The size estimation error of each nanocube causes differences between the measured and simulated spectra. Our FEM simulations show that a size difference ~~of~~ as small as 20 nm leads to a shift of the peaks of about 25 nm. Indeed, the measured spectra of Cube 1 and 2 (Figure 1 (b) and (c)) appear blue-shifted by 20-30 nm. As a consequence, the peaks expected below 400 nm for Cube 1 (Figure 1(f)) is not observed. In case of Cube 2, the expected peak below 400 nm (Figure 1(g)) is observed, but with a reduced intensity. For Cubes 3 and 4, we observe a good agreement between

measurements and simulations, especially below 450 nm. ~~Moreover, since the microscope objectives used in the UV-extended setup are achromats, we observe a reduced sensitivity in the blue range because the focal point of blue doesn't coincide with the common focal point of red and green. For instance, the expected strong peaks close to 400 nm for Cube 1 and 4 (Figure 1(f) and (i)) appear as much smaller peaks in the measured scattering cross-section (Figure 1(b) and (e)).~~ We compare the UV extended setup with a standard previously used dark field spectroscopy setup[10,17] (Figure S3). We observe that the measurement range of UV extended setup is increased down to 350 nm, corresponding to a 90 nm extension of the measurement range. The upper limit of the measurement range is determined by the detection sensitivity limit of the sCMOS camera, which is around 1050 nm. ~~From the comparison between measurement and simulation we also deduce that the sensitivity of the dark field spectroscopy setup drops to zero below 350 nm, thus limiting the measurement range of the setup.~~ A further improvement of the dark field spectroscopy setup in the UV range is challenging because of the lack of objectives which have both a high transmission in the UV range and no chromatic aberrations across the UV to visible range.

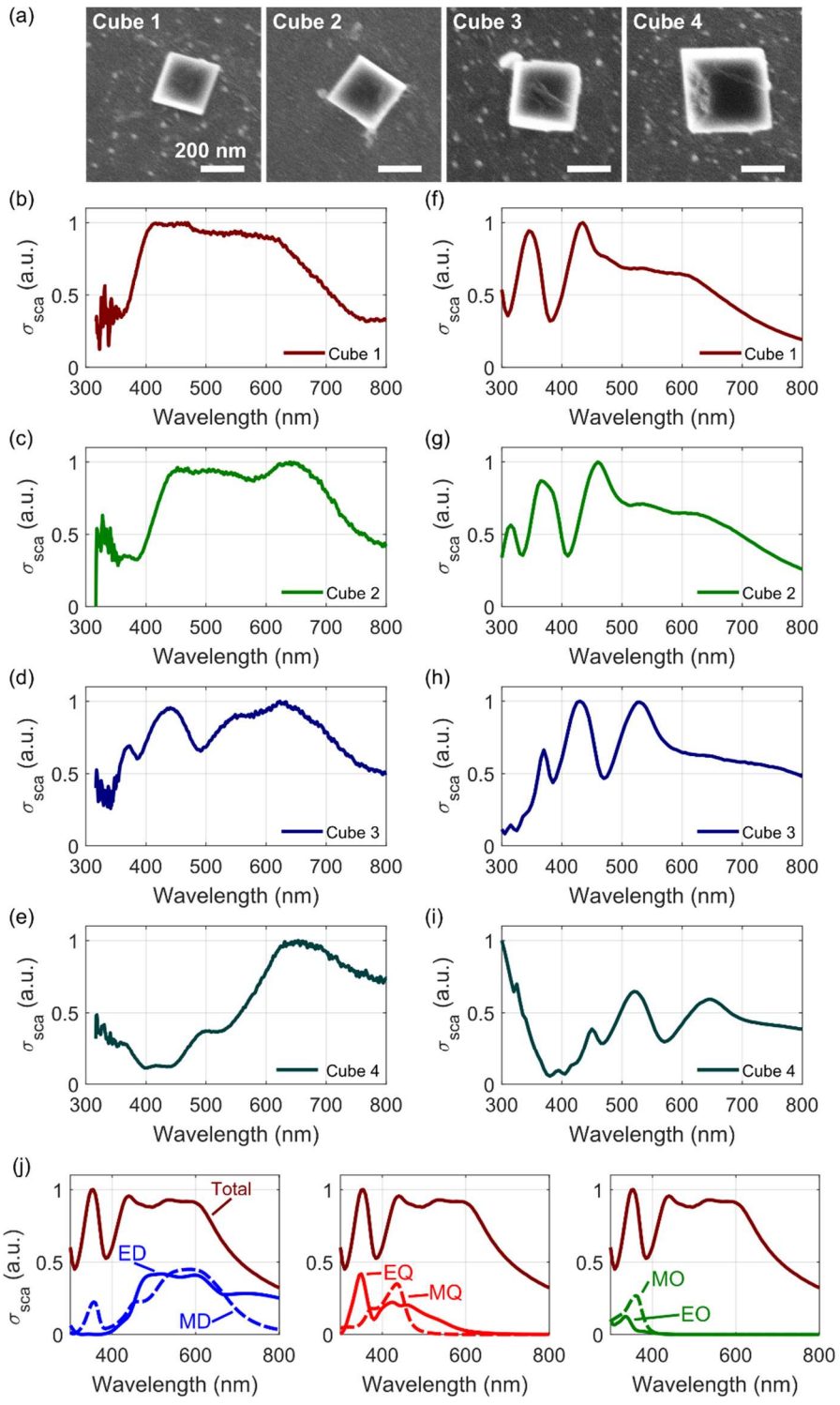

Figure 1: Scattering cross section of single LNO nanocubes (a) SEM micrographs of the isolated single nanocubes (Cube 1, 2, 3 and 4, respectively). (b-e) The measured scattering cross-section

and (f-i) the simulated scattering cross-section of the single LNO nanocubes from (a). The labels indicate the corresponding nanocubes. (j) Spherical multipole expansion calculated with the FEM model from the total scattering cross-section (solid red line) for the LNO nanocube 1. ED – electric dipole , MD – magnetic dipole, EQ – electric quadrupole, MQ – magnetic quadrupole, EO – electric octupole, MO – magnetic octupole.

The results of the spherical multipole expansion is shown in Figure 1(j) for Cube 1 and in Figure S4 for all the other LNO nanocubes presented in this work. For the smaller LNO nanocubes 1 to 3, the linear scattering cross-section continuum between 450 nm and 650 nm is the result of overlapping contributions from the electric and magnetic dipoles and quadrupoles. The peak appearing between 350 and 450 nm consists of overlapping contributions from the magnetic dipole, electric quadrupole and electric and magnetic octupoles. A similar behavior is observed in Cube 4, but, due to its larger size, the peak and the continuum are shifted further in the visible range. The strong overlap between the multipole contributions is a consequence of refractive index value of LNO which, compared to Si, GaAs or Ge, has smaller values (2.4 at 400 nm).[33] This overlap between the magnetic dipole and octopole, and the electric quadrupole in the case of the LNO nanocubes also has a significant impact on the SHG efficiency, as demonstrated in the following section. Finally, in comparison to higher refractive index nanostructures, the scattering cross-section also contains a continuum (for instance, from 450 nm to 600 nm for Cube 1, Figure 1(b)). This makes LNO nanocubes promising structures for broad spectrum applications like spectroscopy.

Second-harmonic generation measurements

As we show that the measured LNO nanocubes scatter light efficiently in the NUV range, we investigate if the nonlinear response from the nanocubes is also strong in this range by measuring

the SHG signal from the individual LNO nanocubes 1 to 4. For this, we use a home-built SHG transmission microscope setup (Figure S5). Prior to full SHG spectra measurements, we show that the signal emitted from a single LNO nanocube consists only of the SHG response by detecting the emission spectrum of a single nanocube with an imaging spectrometer (Figure S6).

First, we measure the SHG spectrum by sweeping the full laser wavelength range from 700 to 1040 nm in steps of 10 nm and recording the corresponding SHG spanning from 350 to 520 nm. We determine the SHG conversion efficiency $\chi_{SHG}^{eff}\gamma$ by dividing the measured SHG ~~irradiance~~ power by the squared laser ~~irradiance~~ power. The values of $\chi_{SHG}^{eff}\gamma$ for all LNO nanocubes 1 to 4 are shown in Figure 2(a-d). The data are normalized to the spectral sensitivity of the experimental setup. The normalization procedure and the calculation of $\chi_{SHG}^{eff}\gamma$ are detailed in Supporting Information, Section 3, where we also estimate the effective second order susceptibility $\chi_{eff}^{(2)}$ (Figure S7). All LNO nanocubes demonstrate efficient SHG emission below 400 nm, particularly the cubes smaller than 300 nm. The measured SHG spectra are also compared to numerical simulations (Figure 2 (e-h)) done with an FEM model. To calculate the SHG from a single LNO cube, we determine the second order polarization from the second order susceptibility tensor $\boldsymbol{\chi}^{(2)}$ (Supporting Information, Section 4) and the electric field distribution of the incident light inside the nanocube. The second order polarization acts as an electromagnetic wave source that radiates into the far field. The SHG power is obtained by integrating the Poynting vector of this source over the solid angle corresponding to the numerical aperture of the collection objective. This method is described in detail in previous works.[17,67] We extended this method by taking the crystal orientation of the LNO nanocube into account (Supporting Informtion, Section 4).

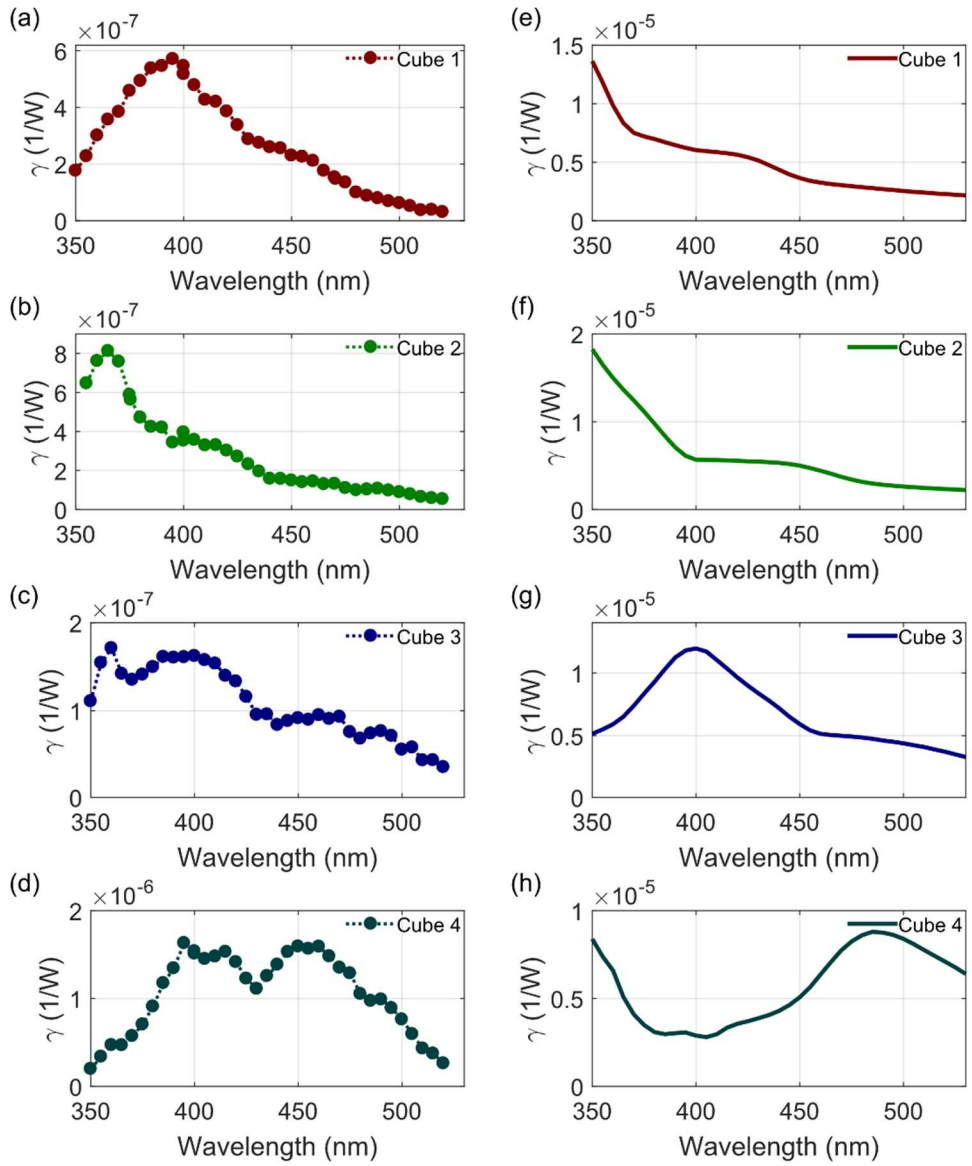

Figure 2: SHG from single LNO nanocubes (a-d) The measured ~~effective~~ SHG conversion efficiency γ and (e-h) the simulated SHG conversion efficiency γ of the single LNO nanocubes from Figure 1(a). The labels indicate to which nanocube the measurement and simulation correspond.

The results of the calculated SHG conversion efficiency γ ~~simulations~~ are shown in Figure 2(e-h) and Figure S4 (thick dotted lines). By comparing the calculated linear scattering cross-section with the calculated SHG ~~intensity~~ conversion efficiency, we observe that the SHG intensity

increases significantly around the Mie resonances consisting of the overlap of four multipole contributions (magnetic dipole, electric quadrupole, electric and magnetic octupoles). Additionally, the SHG ~~intensity~~ conversion efficiency has a shoulder at the overlap between the electric and magnetic quadrupoles (for example, at 425 nm for Cube 1 in Figure S4 (a)). The major features of the calculated SHG spectra are reproduced by the SHG measurements (Figure 2 (a-d)). For Cube 1, 2 and 3 we observe a peak in the SHG intensity from 350 to 450 nm, depending on the cube size, followed by a shoulder and a subsequent faster decrease. However, compared to the calculated values, the SHG peaks of Cube 1 and 4 are red-shifted by 75 nm and blue-shifted by 35 nm, respectively. Here, the estimation error of the LNO nanocube sizes leads to a shift of the peak position of 20 – 30 nm (calculated using the FEM model), which cannot fully explain the significant shift in the case of Cube 1. Furthermore, we observe an additional peak at 400 nm in the SHG spectrum of Cube 4. A likely reason for these discrepancies is the morphology of the LNO nanocubes. For example, Cube 4 (Figure 1(a)) has a defect along one edge, which reduces its geometric symmetry. Also, it cannot be excluded that the nanocubes are formed by two or more single crystals that have maximum SHG emission efficiency at different wavelengths. Nevertheless, all measured LNO nanocubes have significant SHG conversion efficiency values between ~~1.5~~ 1.7 · 10^{-7} 1/W and ~~6.3~~ 7.6 · 10^{-7} 1/W at 360 nm, in the NUV region, for an incident peak irradiance of 1.7 GW/cm^2. The simulation of the SHG conversion efficiency predicts even bigger values around 10^{-5} 1/W for the measured γ. We attribute this difference to multiple causes. First, the LNO nanocube size estimation error causes about 50% variations of the measured γ. Secondly, the excitation in the experiment is done with a focused Gaussian beam, whereas in the simulation we assume a linearly polarized plane wave. Also, any imperfections in the alignment of the SHG measurement setup causes a reduction of the measured γ.

Additionally, we ~~also~~ detect an SHG enhancement value of 10^7 compared to the SHG emitted by bulk LNO at 360 nm. The enhancement calculation procedure is described elsewhere.[10] The efficient SHG emission in the NUV range is therefore another feature of interest of the LNO cube for NUV photonic applications. Moreover, for LNO nanocubes with sizes below 250 nm, the SHG emission in the NUV range is even more efficient than in the visible range. This is a consequence of the refractive index value of LNO. For materials such as LNO, which have a lower refractive index than Si, Ge or GaAs, the electromagnetic field is more confined inside the nanostructure for lower wavelengths that correspond to the higher multipole resonances (Figure S8) where the LNO nanocube interacts more efficiently with the incident electromagnetic field. As the SHG enhancement in harmonic nanoparticles is a consequence of the electromagnetic field confinement in the volume at Mie resonances,[10] the SHG signal in the NUV will be higher than in the visible-infrared.

Due to its tensorial nature, the SHG is highly dependent on the crystal orientation of the material.[54,68] Therefore, we investigate the dependence of the SHG signal on the polarization of the incident laser beam. We rotate the polarization of the incident laser beam using a half-wave plate and we measure the SHG at 400 nm for each LNO nanocube (Figure 3). Remarkably, for all the tested LNO nanocubes, the maximal SHG is obtained when the incident electromagnetic field is polarized along the diagonal of the top face of the LNO nanocube. In the case of Cube 4 (Figure 3(d)), there is a small angular displacement between the diagonal of the top face of nanocube and the axis of the SHG polar plot (Figure 3(d)). This, together with SHG spectrum of Cube 4 (Figure 2(d)), strongly indicate that this cube has morphological defects that lead to the discrepancies of its optical properties compared to Cubes 1 to 3.

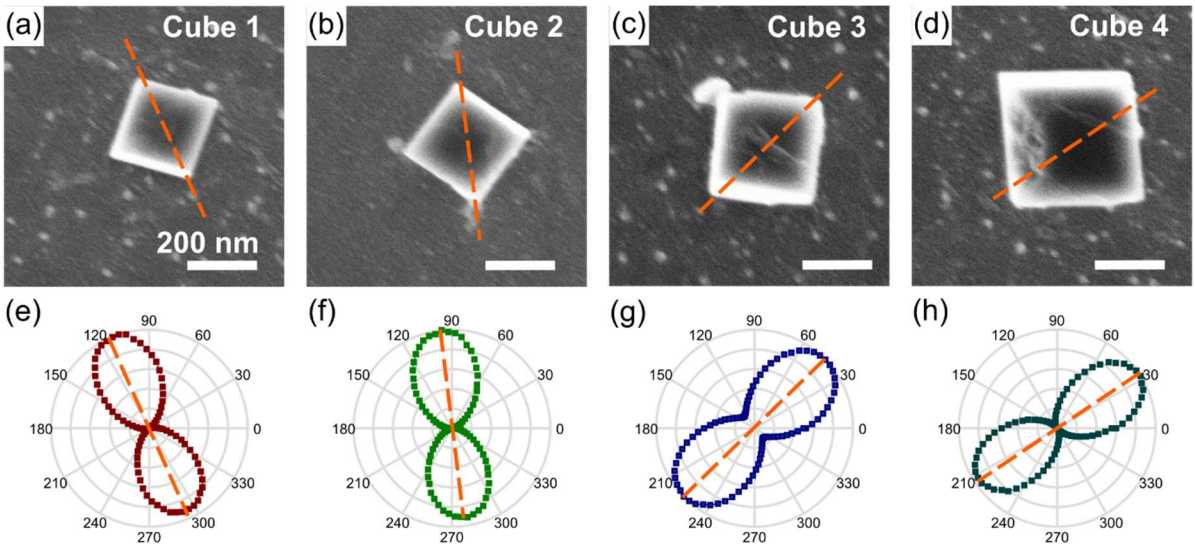

Figure 3: SHG polar plots of single LNO nanocubes (a-d) SEM images of single LNO nanocubes and (e-h) the corresponding SHG polarization dependence at 400 nm. The dashed orange lines serve as a guide to the eye.

The orientation of the SHG polar plots confirms the link between the crystal lattice orientation and the geometrical shape of the LNO nanocubes, which prescribes that the faces of the nanocubes correspond to well-defined families of lattice planes. The polar c-axis of the LNO crystal and the big diagonal of the nanocube are parallel. This indicates that the maximum SHG intensity is obtained when the projection of the incident electromagnetic field on the polar c-axis is maximized. For this particular orientation of the incident electromagnetic field we exploit the d_{33} component of the reduced $\chi^{(2)}$ tensor of LNO, which has a significantly larger value than the rest of the tensor components (-34 pm/V compared to the next closest one -4.88 pm/V, see Supporting Information Section 4). The SHG polarimetry plots combined with the HRTEM measurements (Figure S1(b)) indicate that LNO nanocubes placed on a flat surface have three equivalent orientations depending on which of the (012), (-102) and (1-12) faces the nanocube stands. This

feature increases the control and predictability of the SHG emission for applications, as the randomness of the crystalline orientation typical to spherical nanostructures is not present.

Conclusion

In summary, we show that LNO nanocubes with sizes from 200 to 300 nm have efficient linear and non-linear scattering in the NUV range, with nonlinear conversion efficiencies as large as ~~6.3~~ $7.6 \cdot 10^{-7}$ 1/W and a 10^7 SHG enhancement compared to bulk LNO at 360 nm. Further, we characterized the linear and SHG spectra of single LNO nanocubes both experimentally and numerically, demonstrating their optical properties using the Mie theory formalism. The numerical analysis completed by the spherical multipole expansion of the linear scattering cross-section shows that multiple Mie resonances contribute to the total scattering cross-section and that these resonances are highly tunable with the size of the nanocubes. The high order Mie resonances lead to a strong SHG enhancement that can be achieved in the NUV region for nanocubes with sizes around 200 nm. Furthermore, due to the link between the crystal structure and the geometry of these LNO nanocubes, they have predictable crystal orientation. The LNO nanocubes shown in this work represent a novel material for nonlinear photonics applications like single emitters of sum-frequency generation or single photons sources in the NUV. Moreover, they can serve as building blocks of metasurfaces or composite materials for random scattering in a wider wavelength range that is not accessible with typical semiconductor or other dielectric materials.

Methods

Fabrication of LNO nanocubes. We fabricate LNO powders by a solvothermal synthesis method. We disperse 3 g of Nb2O5 (H.C. Starck, 99.92%) and 0.689 g of LiOH (Aldrich, 98%) in 60 cc of Ethylene Glycol. The suspension is ultrasonicated for 5 min, poured in a PTFE-lined stainless-steel acid digestion bomb (model PA4748, volume 120 mL, Parr Instrument Company)

and hydrothermally treated at 250°C for 70 h. After cooling, the reaction product is washed several times with water. The final powder suspension is then freeze-dried.

UV-extended dark field spectroscopy. We built a dark field spectroscopy setup that has an extended detection range in the UV. The schematic of the UV-extended setup is shown in Figure S2. The light from the xenon arc lamp (150 W, Gilden Photonics) is focused onto the sample using a condenser (Zeiss 20x Epiplan-Neofluar dark field objective with an opaque disk to block the center of the light beam). We place an aperture in front of the lamp to create a virtual light source and avoid imaging the lamp electrodes at the sample position. The light scattered by the sample is collected with a 50x objective (Zeiss 50x Epiplan-Neofluar, NA = 0.55) and detected by a standard CMOS camera and an imaging spectrometer (Princeton Instruments Acton S303 spectrograph) equipped with a CCD camera with an extended UV window (Pixis:256E). The 200 µm core fiber of the imaging spectrometer acts as a pinhole, which allows us to detect only the signal from individual LNO cubes (Figure S2, inset). For each measurement, we adjust the position of single LNO cubes using a CMOS camera. The linear scattering cross-section spectra are obtained by normalizing the signal from a single LNO nanocube to the signal coming directly from the lamp, after subtraction of the background near the LNO nanocube and the dark current counts of the camera.

SHG measurements. We measure the SHG from individual LNO nanocubes using a home-built SHG microscope. The setup is shown in Figure S5. The laser beam from a pulsed Ti:Sapphire laser (Spectra Physics MaiTai DeepSee) is focused onto an LNO nanocube using a lens (f = 25 mm). The SHG and the transmitted laser beam are collected by a 100x objective (Zeiss Neofluar NA = 0.75). The laser beam is removed using a colored glass bandpass filter (Schott BG39) and the SHG signal is measured with a scientific CMOS camera (Andor Zyla 4.2). We control the polarization

of the incident laser beam with a half-wave plate mounted on a motorized rotation stage. We test the emission spectrum from a single nanocube excited by the laser beam to confirm that only SHG is emitted. For this, we measure the signal collected by the objective with an imaging spectrometer (Princeton Instruments Acton S303 spectrograph equipped with a CCD camera Pixis:256E).

Supporting Information: Crystal lattice characterization of LNO nanocubes. UV-extended dark field spectroscopy and SHG measurement setups with spectra normalization procedure and calculation of the effective second order susceptibility. Details about the second order susceptibility tensor of LNO. Electric field maps inside the LNO nanocubes at the Mie resonances. This material is available free of charge online.

Corresponding Author: *ftimpu@phys.ethz.ch

Author Contributions: R.G. and F.T. designed and supervised the experiment. M.T.B. and V.B. fabricated the nanoparticles, performed the XRD and HRTEM measurements. F.T., J.S. and C.R. performed the linear measurements. F.T. performed the nonlinear measurements. F.T. analyzed the data. F.T., L.L. and M.T. carried out the simulations. F.T. wrote the manuscript in collaboration with all the authors. All authors have given approval to the final version of the manuscript.

Funding Sources: The authors acknowledge financial support from the Swiss National Science Foundation grant 150609 and bilateral grant 163916, and the European Research Council starting grant Chi2-Nano-Oxides.

ACKNOWLEDGMENTS

The authors acknowledge the support of the Scientific Center for Optical and Electron Microscopy (ScopeM) of the Swiss Federal Institute of Technology (ETHZ). This work was supported by the Swiss National Science Foundation grant 150609 and bilateral grant 163916 and the European Research Council starting grant Chi2-Nano-Oxides. We thank Adelina Ianculescu, Polytechnic University of Bucharest, for the TEM images of LNO nanocube.

REFERENCES

(1) Sutherland, R. L. *Handbook of Nonlinear Optics*; 2nd editio.; Marcel Dekker, Inc.: New York, 2003; Vol. 35.

(2) Boyd, R. W. *Nonlinear Optics*; Academic Press, 2003.

(3) Houe, M.; Townsend, P. D. An Introduction To Methods of Periodic Poling for Second-Harmonic Generation. *J. Phys. D - Appl. Phys.* **1995**, *28*, 1747–1763.

(4) Baudrier-Raybaut, M.; Haïdar, R.; Kupecek, P.; Lemasson, P.; Rosencher, E. Random Quasi-Phase-Matching in Bulk Polycrystalline Isotropic Nonlinear Materials. *Nature* **2004**, *432*, 374–376.

(5) Suchowski, H.; O'Brien, K.; Jing Wong, Z.; Salandrino, A.; Yin, X.; Zhang, X. Phase Mismatch – Free Nonlinear Propagation in Optical Zero-Index Materials. *Science.* **2013**, *342*, 1223–1226.

(6) Yu, N.; Capasso, F. Flat Optics with Designer Metasurfaces. *Nat. Mater.* **2014**, *13*, 139–150.

(7) Arbabi, A.; Horie, Y.; Bagheri, M.; Faraon, A. Dielectric Metasurfaces for Complete

Control of Phase and Polarization with Subwavelength Spatial Resolution and High Transmission. *Nat. Nanotechnol.* **2015**, *10*, 937–943.

(8) Zheludev, N. I.; Kivshar, Y. S. From Metamaterials to Metadevices. *Nat. Mater.* **2012**, *11*, 917–924.

(9) Bohren, C. F.; Huffman, D. R. *Absorption and Scattering of Light by Small Particles*; John Wiley & Sons, 2008.

(10) Timpu, F.; Sergeyev, A.; Hendricks, N.; Grange, R. Second-Harmonic Enhancement with Mie Resonances in Perovskite Nanoparticles. *ACS Photonics* **2017**, *4*, 76–84.

(11) Liu, S.; Saravi, S.; Keeler, G. A.; Sinclair, M. B.; Yang, Y.; Reno, J.; Pertsch, T.; Brener, I. Resonantly Enhanced Second-Harmonic Generation Using III-V Semiconductor All-Dielectric Metasurfaces. *Nano Lett.* **2016**, *16*, 5426–5432.

(12) Gili, V. F.; Carletti, L.; Locatelli, A.; Rocco, D.; Finazzi, M.; Ghirardini, L.; Favero, I.; Gomez, C. Monolithic AlGaAs Second-Harmonic Nanoantennas. *Opt. Express* **2016**, *24*, 6488–6492.

(13) Carletti, L.; Locatelli, A.; Stepanenko, O.; Leo, G.; Angelis, C. De. Enhanced Second-Harmonic Generation from Magnetic Resonance in AlGaAs Nanoantennas. **2015**, *23*, 26544–26550.

(14) Smirnova, D. A.; Khanikaev, A. B.; Smirnov, L. A.; Kivshar, Y. S. Multipolar Third-Harmonic Generation Driven by Optically Induced Magnetic Resonances. *ACS Photonics* **2016**, *3*, 1468–1476.

(15) Shcherbakov, M. R.; Neshev, D. N.; Hopkins, B.; Shorokhov, A. S.; Staude, I.; Melik-Gaykazyan, E. V.; Decker, M.; Ezhov, A. A.; Miroshnichenko, A. E.; Brener, I.; *et al.* Enhanced Third-Harmonic Generation in Silicon Nanoparticles Driven by Magnetic Response. *Nano Lett.* **2014**, *14*, 6488–6492.

(16) Camacho-Morales, R.; Rahmani, M.; Kruk, S.; Wang, L.; Xu, L.; Smirnova, D. A.; Solntsev, A. S.; Miroshnichenko, A.; Tan, H. H.; Karouta, F.; *et al.* Nonlinear Generation of Vector Beams from AlGaAs Nanoantennas. *Nano Lett.* **2016**, *16*, 7191–7197.

(17) Timofeeva, M.; Lang, L.; Timpu, F.; Renaut, C.; Bouravleuv, A.; Shtrom, I.; Cirlin, G.; Grange, R. Anapoles in Free-Standing III-V Nanodisks Enhancing Second-Harmonic Generation. *Nano Lett.* **2018**, *18*, 3695–3702.

(18) Grinblat, G.; Li, Y.; Nielsen, M. P.; Oulton, R. F.; Maier, S. A. Enhanced Third Harmonic Generation in Single Germanium Nanodisks Excited at the Anapole Mode. *Nano Lett.* **2016**, *16*, 4635–4640.

(19) Miroshnichenko, A. E.; Evlyukhin, A. B.; Yu, Y. F.; Bakker, R. M.; Chipouline, A.; Kuznetsov, A. I.; Luk'yanchuk, B.; Chichkov, B. N.; Kivshar, Y. S. Nonradiating Anapole Modes in Dielectric Nanoparticles. *Nat. Commun.* **2015**, *6*, 1–8.

(20) Butet, J.; Brevet, P. F.; Martin, O. J. F. Optical Second Harmonic Generation in Plasmonic Nanostructures: From Fundamental Principles to Advanced Applications. *ACS Nano* **2015**, *9*, 10545–10562.

(21) Canfield, B. K.; Husu, H.; Laukkanen, J.; Bai, B.; Kuittinen, M.; Turunen, J.; Kauranen, M. Local Field Asymmetry Drives Second-Harmonic Generation in Noncentrosymmetric

Nanodimers. *Nano Lett.* **2007**, *7*, 1251–1255.

(22) Celebrano, M.; Wu, X.; Baselli, M.; Großmann, S.; Biagioni, P.; Locatelli, A.; De Angelis, C.; Cerullo, G.; Osellame, R.; Hecht, B.; *et al.* Mode Matching in Multiresonant Plasmonic Nanoantennas for Enhanced Second Harmonic Generation. *Nat. Nanotechnol.* **2015**, *10*, 412–417.

(23) Butet, J.; Bachelier, G.; Russier-Antoine, I.; Jonin, C.; Benichou, E.; Brevet, P. F. Interference between Selected Dipoles and Octupoles in the Optical Second-Harmonic Generation from Spherical Gold Nanoparticles. *Phys. Rev. Lett.* **2010**, *105*, 1–4.

(24) Khurgin, J. B. How to Deal with the Loss in Plasmonics and Metamaterials. *Nat. Nanotechnol.* **2015**, *10*, 2–6.

(25) Kuznetsov, A. I.; Miroshnichenko, A. E.; Brongersma, M. L.; Kivshar, Y. S.; Luk'yanchuk, B. Optically Resonant Dielectric Nanostructures. *Science.* **2016**, *354*, 846.

(26) Zhao, Q.; Zhou, J.; Zhang, F.; Lippens, D. Mie Resonance-Based Dielectric Metamaterials. *Mater. Today* **2009**, *12*, 60–69.

(27) Decker, M.; Staude, I.; Falkner, M.; Dominguez, J.; Neshev, D. N.; Brener, I.; Pertsch, T.; Kivshar, Y. S. High-Efficiency Dielectric Huygens' Surfaces. *Adv. Opt. Mater.* **2015**, *3*, 813–820.

(28) Jahani, S.; Jacob, Z. All-Dielectric Metamaterials. *Nat. Nanotechnol.* **2016**, *11*, 23–36.

(29) Yang, Y.; Wang, W.; Boulesbaa, A.; Kravchenko, I. I.; Briggs, D. P.; Puretzky, A.; Geohegan, D.; Valentine, J. Nonlinear Fano-Resonant Dielectric Metasurfaces. *Nano Lett.*

2015, *15*, 7388–7393.

(30) Aspnes, D. E.; Studna, A. A. Dielectric Functions and Optical Parameters of Si, Ge, GaP, GaAs, GaSb, InP, InAs, and InSb from 1.5 to 6.0 EV. *Phys. Rev. B* **1983**, *27*, 985–1009.

(31) Baranov, D. G.; Zuev, D. A.; Lepeshov, S. I.; Kotov, O. V.; Krasnok, A. E.; Evlyukhin, A. B.; Chichkov, B. N. All-Dielectric Nanophotonics: The Quest for Better Materials and Fabrication Techniques. **2017**, *4*, 814.

(32) Weber, M. J. *Handbook of Optical Materials*; CRC press, 2002; Vol. 19.

(33) Palik, E. D. Lithium Niobate. In *Handbook of Optical Constants of Solids I*; Academic Press, 1997; pp. 695–702.

(34) Weis, R. S.; Gaylord, T. K. Lithium Niobate: Summary of Physical Properties and Crystal Structure. *Appl. Phys. A Mater. Sci. Process.* **1985**, *37*, 191–203.

(35) Arizmendi, L. Photonic Applications of Lithium Niobate Crystals. *Phys. Status Solidi* **2004**, *201*, 253–283.

(36) Reig Escalé, M.; Sergeyev, A.; Geiss, R.; Grange, R. Nonlinear Mode Switching in Lithium Niobate Nanowaveguides to Control Light Directionality. *Opt. Express* **2017**, *25*, 3013.

(37) Sergeyev, A.; Reig Escalé, M.; Grange, R. Generation and Tunable Enhancement of a Sum-Frequency Signal in Lithium Niobate Nanowires. *J. Phys. D. Appl. Phys.* **2017**, *50*, 044002.

(38) Sergeyev, A.; Geiss, R.; Solntsev, A. S.; Sukhorukov, A. A.; Schrempel, F.; Pertsch, T.; Grange, R. Enhancing Guided Second-Harmonic Light in Lithium Niobate Nanowires. *ACS Photonics* **2015**, *2*, 687–691.

(39) Sergeyev, A.; Geiss, R.; Solntsev, A. S.; Steinbruck, A.; Schrempel, F.; Kley, E.-B.; Pertsch, T.; Grange, R. Second-Harmonic Generation in Lithium Niobate Nanowires for Local Fluorescence Excitation. *Opt. Express* **2013**, *21*, 19012–19021.

(40) Afanasiev, P. Synthesis of Microcrystalline LiNbO3 in Molten Nitrate. *Mater. Lett.* **1998**, *34*, 253–256.

(41) Ali, R. F.; Gates, B. D. Synthesis of Lithium Niobate Nanocrystals with Size Focusing through an Ostwald Ripening Process. *Chem. Mater.* **2018**, *30*, 2028–2035.

(42) Aufray, M.; Menuel, S.; Fort, Y.; Eschbach, J.; Rouxel, D.; Vincent, B. New Synthesis of Nanosized Niobium Oxides and Lithium Niobate Particles and Their Characterization by XPS Analysis. *J. Nanosci. Nanotechnol.* **2009**, *9*, 4780–4785.

(43) Kar, S.; Logad, S.; Choudhary, O. P.; Debnath, C.; Verma, S.; Bartwal, K. S. Preparation of Lithium Niobate Nanoparticles by High Energy Ball Milling and Their Characterization. *Univers. J. Mater. Sci.* **2013**, *1*, 18–24.

(44) Knabe, B.; Buse, K.; Assenmacher, W.; Mader, W. Spontaneous Polarization in Ultrasmall Lithium Niobate Nanocrystals Revealed by Second Harmonic Generation. *Phys. Rev. B - Condens. Matter Mater. Phys.* **2012**, *86*, 1–9.

(45) Liu, M.; Xue, D. A Solvothermal Route to Crystalline Lithium Niobate. *Mater. Lett.* **2005**, *59*, 2908–2910.

(46) Liu, M.; Xue, D.; Luo, C. Facile Synthesis of Lithium Niobate Squares by a Combustion Route. *J. Am. Ceram. Soc.* **2006**, *89*, 1551–1556.

(47) Mohanty, D.; Chaubey, G. S.; Yourdkhani, A.; Adireddy, S.; Caruntu, G.; Wiley, J. B. Synthesis and Piezoelectric Response of Cubic and Spherical LiNbO3 Nanocrystals. *RSC Adv.* **2012**, *2*, 1913.

(48) Wang, Y.; Zhou, X. Y.; Chen, Z.; Cai, B.; Ye, Z. Z.; Gao, C. Y.; Huang, J. Y. Synthesis of Cubic LiNbO3 Nanoparticles and Their Application in Vitro Bioimaging. *Appl. Phys. A* **2014**, *117*, 2121–2126.

(49) Hsieh, C.-L.; Pu, Y.; Grange, R.; Laporte, G.; Psaltis, D. Imaging through Turbid Layers by Scanning the Phase Conjugated Second Harmonic Radiation from a Nanoparticle. *Opt. Express* **2010**, *18*, 20723–20731.

(50) Grange, R.; Lanvin, T.; Hsieh, C.-L.; Pu, Y.; Psaltis, D. Imaging with Second-Harmonic Radiation Probes in Living Tissue. *Biomed. Opt. Express* **2011**, *2*, 2532–2539.

(51) Hsieh, C. L.; Grange, R.; Pu, Y.; Psaltis, D. Three-Dimensional Harmonic Holographic Microcopy Using Nanoparticles as Probes for Cell Imaging. *Opt. Express* **2009**, *17*, 2880–2891.

(52) Staedler, D.; Magouroux, T.; Hadji, R.; Joulaud, C.; Extermann, J.; Schwung, S.; Passemard, S.; Kasparian, C.; Clarke, G.; Germann, M.; *et al.* Harmonic Nanocrystals for Biolabeling: A Survey of Optical Properties and Biocompatability. *ACS Nano* **2012**, *6*, 2542–2549.

(53) Rogov, A.; Mugnier, Y.; Bonacina, L. Harmonic Nanoparticles: Noncentrosymmetric Metal Oxides for Nonlinear Optics. *J. Opt.* **2015**, *17*, 033001.

(54) Timofeeva, M.; Bouravleuv, A.; Cirlin, G.; Shtrom, I.; Soshnikov, I.; Reig Escalé, M.;

Sergeyev, A.; Grange, R. Polar Second-Harmonic Imaging to Resolve Pure and Mixed Crystal Phases along GaAs Nanowires. *Nano Lett.* **2016**, *16*, 6290–6297.

(55) Brasselet, S. Polarization-Resolved Nonlinear Microscopy: Application to Structural Molecular and Biological Imaging. *Adv. Opt. Photonics* **2011**, *3*, 205–271.

(56) Brasselet, S.; Zyss, J. Nano-Crystals for Quadratic Nonlinear Imaging: Characterization and Applications. In *Nanocrystals*; InTech, 2010.

(57) Liu, T. M.; Conde, J.; Lipiński, T.; Bednarkiewicz, A.; Huang, C. C. Revisiting the Classification of NIR-Absorbing/Emitting Nanomaterials for in Vivo Bioapplications. *NPG Asia Mater.* **2016**, *8*, 1–25.

(58) Bonacina, L. Nonlinear Nanomedecine: Harmonic Nanoparticles toward Targeted Diagnosis and Therapy. *Mol. Pharm.* **2013**, *10*, 783–792.

(59) Rogov, A.; Mugnier, Y.; Bonacina, L. Harmonic Nanoparticles: Noncentrosymmetric Metal Oxides for Nonlinear Optics. *J. Opt.* **2015**, *17*, 033001.

(60) Staedler, D.; Magouroux, T.; Hadji, R.; Joulaud, C.; Extermann, J.; Schwung, S.; Passemard, S.; Kasparian, C.; Clarke, G.; Gerrmann, M.; *et al.* Harmonic Nanocrystals for Biolabeling: A Survey of Optical Properties and Biocompatibility. *ACS Nano* **2012**, *6*, 2542–2549.

(61) Staedler, D.; Magouroux, T.; Passemard, S.; Schwung, S.; Dubled, M.; Schneiter, G. S.; Rytz, D.; Gerber-Lemaire, S.; Bonacina, L.; Wolf, J. P. Deep UV Generation and Direct DNA Photo-Interaction by Harmonic Nanoparticles in Labelled Samples. *Nanoscale* **2014**, *6*, 2929–2936.

(62) Mahou, P.; Malkinson, G.; Chaudan, É.; Gacoin, T.; Beaurepaire, E.; Supatto, W. Metrology of Multiphoton Microscopes Using Second Harmonic Generation Nanoprobes. *Small* **2017**, *13*, 1–11.

(63) Akselrod, G. M.; Huang, J.; Hoang, T. B.; Bowen, P. T.; Su, L.; Smith, D. R.; Mikkelsen, M. H. Large-Area Metasurface Perfect Absorbers from Visible to Near-Infrared. *Adv. Mater.* **2015**, *27*, 8028–8034.

(64) Ginn, J. C.; Brener, I.; Peters, D. W.; Wendt, J. R.; Stevens, J. O.; Hines, P. F.; Basilio, L. I.; Warne, L. K.; Ihlefeld, J. F.; Clem, P. G.; *et al.* Realizing Optical Magnetism from Dielectric Metamaterials. *Phys. Rev. Lett.* **2012**, *108*, 1–5.

(65) Liu, S.; Sinclair, M. B.; Mahony, T. S.; Jun, Y. C.; Campione, S.; Ginn, J.; Bender, D. A.; Wendt, J. R.; Ihlefeld, J. F.; Clem, P. G.; *et al.* Optical Magnetic Mirrors without Metals. *Optica* **2014**, *1*, 250.

(66) Marino, G.; Solntsev, A. S.; Xu, L.; Gili, V.; Carletti, L.; Poddubny, A. N.; Smirnova, D.; Haitao, C.; Zhang, G.; Zayats, A. V.; *et al.* Sum-Frequency Generation and Photon-Pair Creation in AlGaAs Nano-Disks. In *2017 Conference on Lasers and Electro-Optics Europe & European Quantum Electronics Conference (CLEO/Europe-EQEC)*; IEEE: Munich, 2017; pp. 1–1.

(67) Timpu, F.; Hendricks, N. R.; Petrov, M.; Ni, S.; Renaut, C.; Wolf, H.; Isa, L.; Kivshar, Y.; Grange, R. Enhanced Second-Harmonic Generation from Sequential Capillarity-Assisted Particle Assembly of Hybrid Nanodimers. *Nano Lett.* **2017**, *17*, 5381–5388.

(68) Hsieh, C.-L.; Pu, Y.; Grange, R.; Psaltis, D. Second Harmonic Generation from

Nanocrystals under Linearly and Circularly Polarized Excitations. *Opt. Express* **2010**, *18*, 11917–11932.